

Distributed modeling and torque transmission analysis of a cable-driven robotic joint

| | |
|---------------|---|
| Authors | Li, Yu;Sadeghian, Hamid;Forouhar, Moein;Naceri, Abdeldjallil;Haddadin, Sami |
| Citation | Y. Li, H. Sadeghian, M. Forouhar, A. Naceri, S. Haddadin, "Distributed modeling and torque transmission analysis of a cable-driven robotic joint," <i>Mechatronics</i> , vol. 117, pp. 103517-103517, 2026, https://doi.org/10.1016/j.mechatronics.2026.103517 . |
| DOI | 10.1016/j.mechatronics.2026.103517 |
| Publisher | Elsevier |
| Download date | 2026-06-07 05:07:33 |
| Item License | http://creativecommons.org/licenses/by/4.0/ |
| Link to Item | https://hdl.handle.net/20.500.14634/2294 |



Distributed modeling and torque transmission analysis of a cable-driven robotic joint^{☆,☆☆}

Yu Li^a ^{*}, Hamid Sadeghian^a, Moein Forouhar^a , Abdeldjallil Nacéri^a, Sami Haddadin^b

^a Munich Institute of Robotics and Machine Intelligence, Technical University of Munich, Munich, Germany

^b Mohamed Bin Zayed University of Artificial Intelligence, Abu Dhabi, United Arab Emirates

ARTICLE INFO

Keywords:

Cable-driven systems
Distributed modeling
Tendon–sheath transmission
Friction–elasticity modeling
Hysteresis

ABSTRACT

Cable-driven actuation provides spatial flexibility for remote power transmission and offers inherent mechanical compliance. However, torque transmission is compromised by coupled nonlinear phenomena, including distributed friction, curvature-induced normal forces, pretension redistribution, and elasticity-induced hysteresis. Existing models typically address only a subset of these effects or depend on empirical mappings, thereby limiting their predictive accuracy for torque-level integration. In this work, we model a dual-cable tendon–sheath transmission as a bidirectionally coupled dynamic subsystem and develop a distributed spring–friction–unit formulation that explicitly links routing geometry, pretension, and distal dynamics to transmitted torque, hysteresis, and apparent stiffness variation. To facilitate practical deployment, we derive a reduced analytical representation through model-order reduction combined with a curvature-informed averaged-pretension approximation, and assess its validity via discretization-sensitivity analysis. Experiments on two dedicated dual-cable joint testbeds validate torque prediction across diverse routing and loading conditions and demonstrate partial feedforward friction compensation that enhances interaction transparency. Practical limitations and deployment considerations are also discussed.

1. Introduction

Cable-driven actuation systems have become prevalent in robotics, including soft manipulators [1], upper-limb exoskeletons [2,3], parallel platforms [4], and surgical end-effectors [5]. These systems are generally categorized as pure tendon-driven or tendon–sheath-driven. The latter introduces a compliant sheath, enhancing cable-routing flexibility, passive compliance, and physical Human–Robot Interaction (pHRI) capability [6,7], especially advantageous in Remote Actuation Systems (RAS) that decouple the actuator from the joint, reducing distal mass and enabling compact or wearable configurations [6].

Compared to rigid capstan-driven mechanisms, tendon–sheath systems allow free cable paths within limited spaces, but introduce significant nonlinear transmission disturbances. Particularly problematic are friction under tension, cable elasticity, and stick–slip dynamics [8,9], which strongly depend on cable routing, pretension, and envi-

ronmental interactions. Such disturbances complicate accurate torque transmission and transparent control.

Different cable actuation modes produce friction through distinct mechanisms. Linear (pull-only) transmission systems generate friction primarily via input tension amplified by cable bending [10,11]. In contrast, torsional (pull–pull/pull–push) systems can exhibit friction arising mainly from internal pretension interacting with cable bending. In this work, we focus on the pretensioned pull–pull regime with no slack, which is less directly influenced by input torque [12]. Further complexities arise from cable material and geometry. Thin, low-tension tendons often exhibit near-Coulomb behavior and can be approximated by threshold-type compensation [13,14], whereas thicker cables (as used in this work) exhibit pronounced interface adhesion and non-trivial tension propagation [15]. These characteristics motivate modeling approaches that explicitly account for curvature-dependent loading and spatially distributed transmission effects, beyond purely lumped input–output friction representations.

[☆] This paper was recommended for publication by Associate Editor Tom Oomen.

^{☆☆} The authors would like to thank the Federal Ministry of Research, Technology, and Space (BMFTR) for its support as part of the research program Communication Systems “Souverän. Digital. Vernetzt”. Joint project 6G-life, project identification number: 16KIS2414. We gratefully acknowledge the funding of the Lighthouse Initiative Geriatrics by LongLeif GaPa gGmbH (Project Y) and funding from the European Union’s Horizon Europe research and innovation programme as part of the project FlexCycle under grant agreement No. 101189600.

^{*} Corresponding author.

E-mail address: yu.li@tum.de (Y. Li).

Table 1
Summary of Key Transmission Effects in Tendon–Sheath Systems.

| No. | Effects factor | Notation | Extent interpretation | Physical mechanism and consequence | Reference |
|-----|----------------------|------------------|---|---|------------|
| 1 | Bending shape | κ, θ | Higher friction with increased bending | Alters normal force distribution along sheath interface | [16,19,20] |
| 2 | Pre-tension | T_0 | Higher friction with increased pretension | Primary source of normal force generation | [12,16] |
| 3 | Effective Stiffness | k | Less hysteresis with increased rigidity | Accelerates propagation of transmission dynamics | [16,18] |
| 4 | Environment dynamics | τ_{out} | Reduced backlash with increased environment dissipation | Environment stiffness modulates torque backlash amplitude | This work |
| 5 | Diameter deviation | – | Increased pretension variation with greater deviation | Loose tendon–sheath fitting amplifies coupling between bending and pretension | [21] |

Prior first-principles distributed transmission models [16,17] improve physical interpretability but often rely on simplified cable properties or fixed routing assumptions, which can reduce predictive accuracy under varying configurations [18]. Moreover, the equivalent effective tendon–sheath stiffness is frequently oversimplified. In practice, stiffness depends intricately on pretension and cable shape, while the nonlinear coupling of these factors remains insufficiently characterized.

Collectively, cable bending, pretension redistribution, stiffness variation, and joint-side interaction constitute what we refer to as *transmission effects*. In this work, we focus on torsional dual-cable tendon–sheath systems and investigate how these effects emerge jointly rather than in isolation. Table 1 summarizes their physical origins and consequences.

While previous studies have individually addressed friction, elasticity, and pretension effects, a unified model explicitly capturing their coupled interactions remains lacking. To address this, we propose a distributed transmission modeling framework for dual-cable tendon–sheath systems, explicitly revealing how cable shape, pretension distribution, and distal dynamics collectively shape the torque transmission and elastic frictional behaviors. Specifically, our *contributions* are:

1. A physics-informed distributed modeling framework for dual-cable transmissions that captures the coupled effects of curvature-dependent friction and cable elasticity, enabling explicit analysis of pretension evolution and torque transmission limits along curved routing paths.
2. A curvature-informed effective pretension formulation that reveals how non-uniform tension distributions govern output torque, together with an averaging strategy that yields discretization-robust torque prediction without requiring fine spatial resolution. This results in a reduced-order analytical description suitable for system-level analysis and practical use.
3. Experimental validation on two dedicated testbeds, separating modeling verification from application-oriented evaluation. The proposed reduced model is integrated into a representative joint torque application involving human interaction, experimentally highlighting elasticity-induced torque degradation that cannot be explained by lumped transmission models.

2. Related work

Modeling of tendon–sheath transmissions has progressed from empirical characterization to analytical mappings and, more recently, distributed and learning-based formulations. Across these lines, curvature-dependent normal loading, pretension, and elasticity are consistently identified as dominant sources of hysteresis and torque loss.

Early work established key phenomena in tendon-driven transmissions, including shape/pretension-dependent friction, backlash-like hysteresis, and stiction-induced oscillations [19,22,23]. Continuum perspectives were later introduced to relate spatial effects to dynamic behavior [24]. However, these studies did not provide a unified quantitative link between routing geometry, pretension, and distal-side dynamics.

For deployment, analytical transmission mappings remain common approach. Wu et al. [12] derived torque to displacement relations under simplified geometry/pretension assumptions; extensions incorporate non-uniform tension and fitting effects for improved practicality [21,25]. Their applicability can degrade when pretension becomes strongly non-uniform under thick-cable adhesion and routing heterogeneity [16].

Distributed formulations explicitly resolve transmission dynamics by discretizing the path and enforcing tension/friction consistency along the routing [16,18]. Later variants improve interaction modeling or introduce distributed internal friction states, but often rely on additional sensing or simplified geometry, and do not always reduce cleanly to deployable forms [17,26].

Beyond physics-based modeling, lumped hysteresis operators and learning-based approaches provide compact input–output representations, but do not natively encode curvature-dependent loading or arc-length pretension fields and may sacrifice interpretability/generalization across routings [27–29]. Many control-oriented implementations further embed transmission effects into effective stiffness and friction terms, effectively treating the transmission as a memoryless torque channel [21,30].

In contrast, the present work clarifies how friction, elasticity, pretension, and geometry jointly shape transmission behavior within a unified, physically interpretable framework, and bridges a distributed model with a deployable reduced representation.

Model-class distinction and comparison scope. For tendon–sheath transmissions, comparisons are most informative when model classes are distinguished before selecting quantitative baselines. *Lumped hysteresis operators* (e.g., LuGre or Bouc–Wen) compactly reproduce hysteresis phenomenology but do not explicitly represent curvature-dependent loading, spatial pretension fields, or bidirectional dual-cable coupling (Table 2). Quantitative benchmarking against such operators would require introducing additional geometric or pretension states that are not directly measurable in typical deployments, effectively changing the model class. Accordingly, lumped operators are used here only for qualitative discussion of hysteresis shaping rather than as primary quantitative baselines.

Analytical transmission mappings (Wu/Jung-type) constitute a well-posed baseline for deployment-oriented comparison. In this work, these mappings are shown to arise as a closed-form special case of the proposed distributed model under model-order reduction and averaged

Table 2

Model-class capability matrix for dual-cable tendon–sheath transmissions. Entries indicate whether a capability is supported by the model family under its standard assumptions, without introducing additional unmodeled states or ad-hoc inputs.

| Model family | Spatial states | Curvature-dependent normal load | Pretension field | Dual-cable bidirectional coupling | Analytical reduction | Deployment w/o internal sensing |
|---|----------------|---------------------------------|-----------------------|-----------------------------------|----------------------|--------------------------------------|
| Lumped friction/hysteresis (LuGre, Bouc–Wen) | No | No | No | No | No | Yes |
| Analytical transmission mappings (Wu/Jung-type) | No (global) | No | Yes (scalar/averaged) | Yes | Yes | Yes |
| Distributed continuum/discretized models (Agrawal-type, Palli-type) | Yes | Yes | Yes | Often partial/single-cable focus | Not always | Not always |
| This work (spring–friction units, dual-cable subsystem) | Yes | Yes | Yes | Yes | Yes (MoR) | Yes (via averaged pretension) |

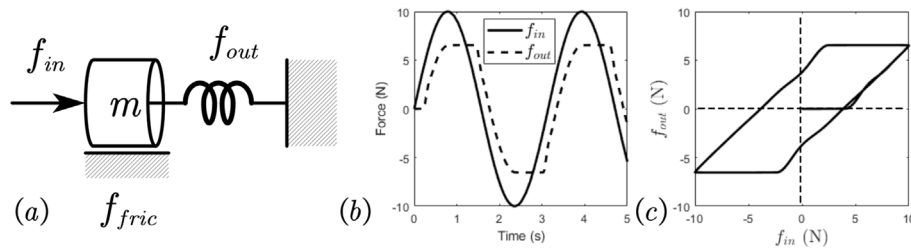


Fig. 1. (a) Unit spring–friction model representing transmission hysteresis. (b) Saturated output under sinusoidal input. (c) Hysteresis loop with stick–slip transition.

pretension assumptions (Sections 3.3, 4.4.2). Quantitative baselines within this class are provided in Fig. 11 using a consistent friction coefficient and parameter identification protocol.

Finally, *distributed continuum or discretized transmission models* (Agrawal-type, Palli-type, and related variants) are the closest methodological baseline to our full-order formulation, since they also resolve spatially distributed frictional losses under curvature-dependent normal loading. Our framework departs from these foundations mainly in the friction–tension coupling primitive and, consequently, in how hybrid stick–slip behavior is represented.

Agrawal-type discretizations typically combine (i) a capstan-like tension transfer relation within moving segments and (ii) an explicit regime resolution (e.g., stick, slip and/or partial motion) that requires segment-/node-level bookkeeping to determine which portions move and which stick. Palli-type models extend this line by introducing distributed internal friction states (e.g., LuGre/Dahl) along the sheath, but their numerical evaluation still depends on consistent regime evolution and on sensing/parameterization choices for internal states. In contrast, our formulation embeds the stick–slip mechanism into a minimal local spring–friction unit: friction enters as an internal force term within the same distributed state evolution, avoiding node-wise regime selection and supporting systematic reduction. In particular, commonly used analytical transmission mappings (Wu/Jung-type) can be interpreted as closed-form special cases obtained from our distributed model under model-order reduction together with an averaged-pretension approximation (Sections 3.3, 4.4.2).

This work focuses on the pretensioned pull–pull actuation regime and assumes strictly positive tension without slack during operation. We also incorporate distal-side load dynamics through the boundary condition, so that output-side dissipation influences the internal transmission states and the observed time-domain transmissibility within the operating regime considered here. Accordingly, we organize comparisons by structure-consistent criteria (Table 2) about how friction–tension coupling is represented, how pretension is treated, what boundary/load coupling is assumed, whether a deployable reduction exists,

and what sensing is required, rather than enforcing parameter matching across model classes with incompatible measurement assumptions.

3. Modeling

We model the dual-cable tendon–sheath transmission as an independent distributed subsystem to expose how curvature-dependent loading and pretension affect on torque loss and hysteresis. A discretized full-order model is derived from a local unit and systematically reduced to a deployable analytical form.

Scope and geometric assumptions. Throughout this paper, the tendon–sheath routing is treated as a prescribed geometric input represented by an arc-length-parameterized centerline curvature profile. The proposed formulation targets axial torque transmission effects dominated by curvature-induced normal loading, distributed friction, and cable elasticity under a pretensioned pull–pull operating regime (no slack). The routing is assumed mechanically constrained by the device structure so that load-induced routing deformation is negligible within the considered excitation range. Accordingly, the model focuses on axial transmission along the given routing, with routing compliance effects absorbed into the prescribed geometry used as input.

3.1. Spring–friction-unit representation

To introduce the minimal internal state required to reproduce transmission hysteresis, we begin with a basic 1-DOF spring–friction unit, illustrated in Fig. 1(a). The unit is not intended as a complete cable model, but as a conceptual abstraction of local transmission behavior, where an internal deformation state mediates the relation between input and output forces.

Under this representation, the input force f_{in} is not directly transmitted to the output f_{out} . Instead, the difference $f_{in} - f_{out}$ is absorbed

by the internal state through elastic deformation and frictional dissipation. This structure gives rise to a backlash-like hysteresis: the output remains unchanged until the internal state overcomes the friction threshold, after which motion and force transmission resume.

The governing dynamics of the unit is given by

$$f_{in} - f_{out} - f_{fric} = m\ddot{x}, \quad (1)$$

where x denotes the internal transmission state and f_{fric} represents dry friction. As shown in Fig. 1(b), the output force saturates under periodic input due to friction. The corresponding hysteresis loop in Fig. 1(c) highlights that force transmission is regulated by the internal state rather than by direct input–output mapping. This minimal structure serves as the conceptual template for the distributed transmission model developed in the following, where multiple of such internal transmission states emerge naturally along the cable path due to elasticity, friction, and curvature.

3.2. Distributed transmission model (full order)

3.2.1. Tendon–sheath model

The transmission consists of two antagonistic cables routed through flexible sheaths and connected to input and output pulleys, as illustrated in Fig. 2(a). Each cable is discretized into finite segments, where elastic deformation and frictional interaction with the sheath give rise to distributed internal transmission states (Fig. 2(b,c)). Segment inertia is neglected due to the low cable mass density, while small viscous damping is introduced solely for numerical regularization.

The upper cable includes N internal nodes (x_1 to x_N) and two boundary nodes (x_0, x_{N+1}), connected by $N + 1$ serial springs. The lower cable uses the same scheme, with nodes indexed from x_{N+2} to x_{2N+3} . The resulting system comprises distributed internal transmission states for both cables, boundary states associated with pulley motion, and two pulley coordinates driven by the input and output torques. The pulley coordinates q_{in} and q_{out} are included explicitly to represent the boundary excitation; cable segment displacements are initialized with non-zero offsets to impose pretension.

3.2.2. Discretized transmission dynamics

We derive a massless, first-order transmission model for the dual cable system from the input pulley through the segmented cable to the output pulley. The governing equations are:

$$\begin{aligned} -\tau_{in} + b_{in}\dot{q}_{in} + k(x_0 - x_1)r_{in} \\ -k(x_{2N+2} - x_{2N+3})r_{in} &= 0, \end{aligned} \quad (2)$$

$$b_i\dot{x}_i - k(x_{i-1} - x_i) + k(x_i - x_{i+1}) + f_{fric,i} = 0, \quad (3)$$

$$\begin{aligned} b_{out}\dot{q}_{out} + k_{out}q_{out} - k(x_N - x_{N+1})r_{out} \\ -k(x_{N+2} - x_{N+3})r_{out} &= 0, \end{aligned} \quad (4)$$

The associated tension and torque observations are,

$$f_{i-1,i} = k(x_{i-1} - x_i), \quad (5)$$

$$\tau_{out} = k(x_N - x_{N+1})r_{out} + k(x_{N+2} - x_{N+3})r_{out}. \quad (6)$$

Here, τ_{in} is the commanded input torque. Pulley inertias are neglected. The damping b_{in} preserves the torsional coordinate q_{in} , making τ_{in} the system input. All spring constants k are assumed uniform. Output dynamics include dissipative and potential effects via b_{out} and k_{out} . Node friction $f_{fric,i}$ is defined in Section 3.2.3. Eq. (3) holds for all $i \in [1, N] \cup [N + 3, 2N + 2]$, covering $2N$ internal states.

Eqs. (2)–(4) define a distributed transmission dynamics with linear elastic coupling and nonlinear nodewise friction, while (5) and (6) provide physically meaningful tension and torque observations. The transmission state-space and output representations are

$$\mathbf{B}\dot{\mathbf{x}}_{\text{trs}} + \mathbf{K}\mathbf{x}_{\text{trs}} = \mathbf{D}_{in}\tau_{in} + \mathbf{D}_{bdry}\mathbf{x}_{bdry} - \mathbf{f}_{fric}, \quad (7)$$

$$\begin{aligned} \mathbf{f} &= \mathbf{H}_{\text{trs}}\mathbf{x}_{\text{trs}} + \mathbf{H}_{bdry}\mathbf{x}_{bdry}, \\ &= [\dots, f_{i,i-1}, \dots, \tau_{out}]^T \in \mathbb{R}^{2N+1}, \end{aligned} \quad (8)$$

where $\mathbf{x}_{\text{trs}} \in \mathbb{R}^{2N+2}$ collects the internal dynamic states as $[q_{in}, \mathbf{x}^{(1)}, \mathbf{x}^{(2)}, q_{out}]$ with

$$\mathbf{x}^{(1)} := [x_1, \dots, x_N]^T, \quad \mathbf{x}^{(2)} := [x_{N+3}, \dots, x_{2N+2}]^T.$$

and $\mathbf{x}_{bdry} = [x_0, x_{N+1}, x_{N+2}, x_{2N+3}] \in \mathbb{R}^4$ denotes the boundary displacement states driven by the pulley coordinates via (9). Matrices \mathbf{B} and \mathbf{K} are damping and stiffness, \mathbf{D}_{bdry} couples boundary inputs, and \mathbf{f}_{fric} collects the friction terms. The input matrix is $\mathbf{D}_{in} = [1, \mathbf{0}_{1 \times (2N+1)}]^T$, and $\mathbf{H}_{\text{trs}}, \mathbf{H}_{bdry}$ retain the k occupancy of entries following (5) and (6).

Initial cable pretension is imposed via the initial displacement $x_i(0)$ for $i \in [0, 2N + 3]$. The coupling between pulley coordinates and cable boundaries are,

$$\begin{aligned} x_0(t) &= x_0(0) + q_{in}(t)/r_{in}, \\ x_{N+1}(t) &= x_{N+1}(0) + q_{out}(t)/r_{out}, \\ x_{N+2}(t) &= x_{N+2}(0) + q_{out}(t)/r_{out}, \\ x_{2N+3}(t) &= x_{2N+3}(0) + q_{in}(t)/r_{in}. \end{aligned} \quad (9)$$

3.2.3. Sheath friction node

When the cable is straight, the tendon ideally lies along the centerline of the sheath without contact. However, under bending and tension, the tendon is pressed against the inner wall of the curved sheath, generating a normal force f_N as illustrated in Fig. 2(d). An infinitesimal analysis yields,

$$f_N = f \sin\left(\frac{d\theta}{2}\right) + (f + \Delta f) \sin\left(\frac{d\theta}{2}\right), \quad (10)$$

where $d\theta$ is the infinitesimal bending angle, and $f, \Delta f$ are the tension and its differential. Using $d\theta = \kappa(s)ds$ with s denoting the physical arc-length coordinate along the sheath centerline,

$$f_{N,i} = \frac{(f_{i-1,i} + f_{i,i+1})l_i}{2r_i} = \frac{(f_{i-1,i} + f_{i,i+1})}{2}\theta_i, \quad (11)$$

where $\theta_i = \int_{s_{i-1}}^{s_i} \kappa(s)ds$ is the accumulated bending angle over segment i with segment length $l_i = s_i - s_{i-1}$. Under the segment-wise constant-curvature (SCC) assumption, $\kappa(s) \approx \kappa_i$ on segment i , yielding $\theta_i \approx \kappa_i l_i$ with $r_i := 1/\kappa_i$, i.e., $\theta_i \approx l_i/r_i$. The SCC assumption is adopted to enable a tractable discretization of the transmission geometry and does not constitute a fundamental physical requirement of the proposed formulation.

Generally, such node's friction can be represented by a velocity dependent representation as,

$$f_{fric,i} = \mu(\dot{x})f_{N,i}, \quad (12)$$

where $\mu(\dot{x})$ can present some velocity-dependent friction coefficient. In practice, to improve numerical robustness and avoid massive velocity feedback for large N , we replace the discontinuous Coulomb friction term with a continuous, velocity-independent formulation based on a smooth sign-function variant:

$$f_{fric,i}(f_{in,i}) = \frac{\mu f_{N,i} \epsilon_i}{(1 + |\epsilon_i|^p)^{1/p}}, \quad (13)$$

where

$$\epsilon_i = \frac{f_{in,i}}{\mu f_{N,i}}, \quad f_{in,i} = f_{i-1,i} - f_{i,i+1}.$$

Here $f_{N,i}$ is the local normal force at node i , $\mu > 0$ is the constant friction coefficient, and p controls the steepness of the transition between static and sliding regimes (see Fig. 3). The normalized variable ϵ_i represents the ratio of the net tangential force to the local Coulomb limit $\mu f_{N,i}$, such that $|\epsilon_i| < 1$ corresponds to the sticking region and $|\epsilon_i| \gg 1$ approaches the kinetic regime. Because ϵ_i carries the sign of motion tendency, the formulation inherently encodes directionality without relying on velocity measurements. This regularization yields a smooth Coulomb-like response that avoids numerical chattering and remains well-defined even at zero velocity.

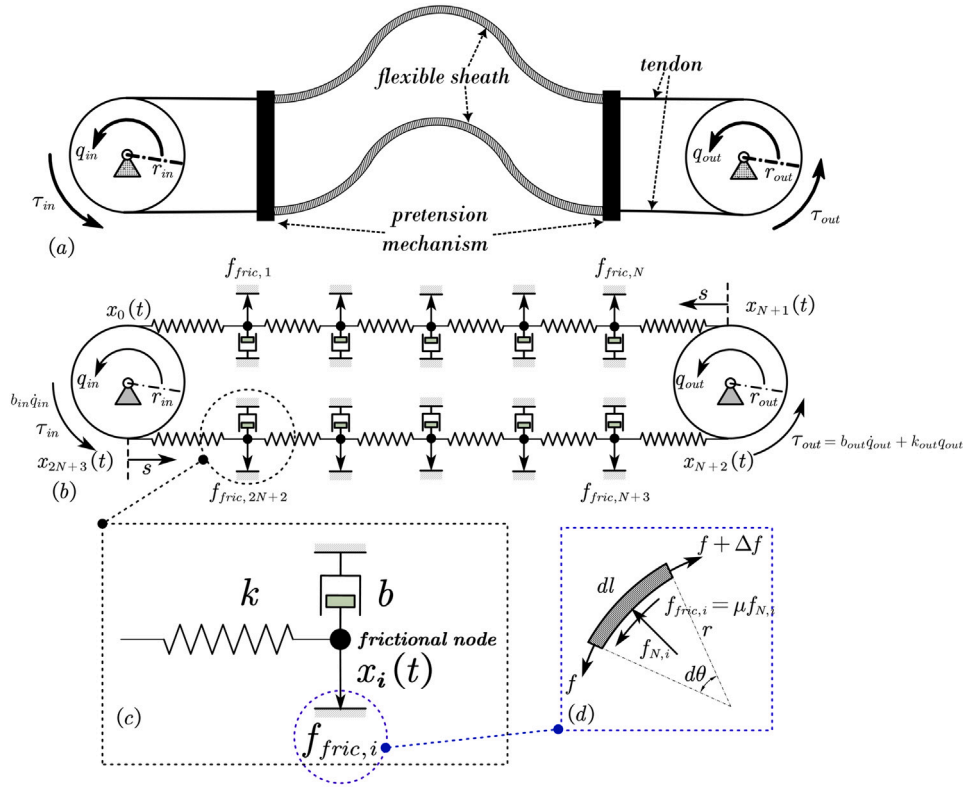


Fig. 2. Decomposition of a dual cable system. (a) Dual cable-pulley mechanism consists of flexible-sheath, tendons, and pretension mechanism as fixing fixture. (b) Dual cable model with input–output pulleys and coordinate convention with discretization of tendon–sheath into spring–damper junction elements connection. The output side is modeled as a passive linear impedance (Section 4.3.4); a small input-side damping is used for numerical regularization. (c) A spring–damping unit parameterized by constant k , b_i , and dry friction $f_{fric,i}$. (d) Quasi-static analysis of one segment.

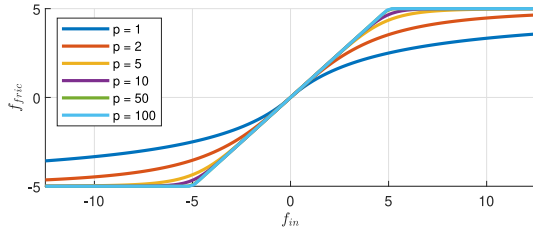


Fig. 3. Smooth approximation of Coulomb-like friction with varying exponent p . A sharp approximation selection of $p = 100$ was applied throughout.

3.3. Reduced to analytical transmission model

To enable analytical interpretation and deployment, we consider a reduced-order case with $N = 1$, which retains a single internal transmission state while preserving the input–output separation and hysteresis mechanism of the distributed model.

From (2)–(4) and Fig. 2, the reduced case gives

$$\tau_{in} = r_{in}(f_{0,1} - f_{4,5}), \quad (14)$$

$$\tau_{out} = r_{out}(f_{1,2} - f_{3,4}), \quad (15)$$

leading to

$$\tau_{out} = \frac{r_{out}}{r_{in}} \tau_{in} - r_{out} f_b - \tau_{f,c}, \quad (16)$$

where $f_b = b_1 \dot{x}_1 + b_4 \dot{x}_4$ is a small unobserved damping term, and $\tau_{f,c} = r_{out}(f_{fric,1} + f_{fric,4})$ is the total friction torque.

To eliminate internal states in $\tau_{f,c}$, we use boundary-displacement tension sums:

$$f_{0,1} + f_{1,2} = k \left(\frac{q_{in}}{r_{in}} + x_0(0) - \frac{q_{out}}{r_{out}} - x_2(0) \right), \quad (17)$$

$$f_{3,4} + f_{4,5} = k \left(\frac{q_{out}}{r_{out}} + x_3(0) - \frac{q_{in}}{r_{in}} - x_5(0) \right). \quad (18)$$

With the curvature-based friction model (12),

$$\begin{aligned} \tau_{f,c} &= \frac{\mu\theta}{2} (f_{0,1} + f_{1,2} + f_{3,4} + f_{4,5}) r_{out}, \\ &= \mu\theta k (x_0(0) - x_2(0)) r_{out}, \end{aligned} \quad (19)$$

where the pretension terms reflect the static equilibrium imposed at initialization. In practice, the individual pretension contributions from both cables enter the transmission torque additively and can be estimated independently, as discussed in Section 4.4.2. Under the proposed curvature–pretension formulation, the resulting reduced analytical transmission law recovers the Wu/Jung-type representation [12,21] as a special case.

For practical deployment under limited sensing, the reduced transmission is rewritten in a torsional unit form that preserves the internal transmission structure introduced in Fig. 1(a). Specifically, the residual term $r_{out} f_b$ in (16) is absorbed into an equivalent torsional state, yielding

$$\tau_{in} - \tau_{out} - \hat{\tau}_{fric} = \gamma \dot{q}, \quad (20)$$

with $\tau_{out} = k_{out} q + b_{out} \dot{q}$. Here, γ denotes an equivalent stabilized inertia introduced for numerical regularization, distinct from the massless distributed assumption. The friction magnitude $\tau_{f,c}$ can be imposed into the torsional dynamics by adapting it into Stribeck–Coulomb–damping variant that preserves the sticky friction.

$$\hat{\tau}_{f,c} = \tanh(\alpha \dot{q}) [\zeta_c + (\zeta_s - \zeta_c) e^{-|\dot{q}/\eta_s|^2}] \tau_{f,c} + b_{vis} \dot{q}, \quad (21)$$

Table 3
Model Parameter Summary.

| Symbol | Interpretation | Unit | Value/Source |
|--------------|----------------------------|---------|--------------|
| κ | Curvature | 1/mm | Recorded |
| b_{in} | Motor damping | Nms/mm | 1e-4 |
| b_l | Cable damping | Ns/mm | 1e-3 |
| b_{out} | Output damping | Nms/rad | - |
| k | Cable segment stiffness | N/mm | - |
| k_{out} | Output stiffness | Nm/rad | - |
| μ | Cable friction coefficient | - | 0.052 |
| $r_{in/out}$ | Input-output pulleys radii | mm | 40 |

where $\tau_{f,c}$ is the nominal reduced-model friction torque from (19). The parameters $\zeta_s \geq \zeta_c = 1$ scale sticky effects locally, b_{vis} represents additional viscous damping effect, and α, η_s tune the transition steepness and velocity sensitivity. The torsional transmission state q thus decouples input-output dynamics while preserving the hysteresis structure inherited from the distributed formulation.

4. Results

In this section, we evaluate stiffness/hysteresis trends, quantify torque prediction across routings and discretizations, and finally validate a deployment-oriented friction feedforward use case on two testbeds.

4.1. Dual-cable tendon-sheath transmission testbed

The experimental platform comprises an input pulley, an output pulley, and a closed-loop dual Bowden-cable transmission (Fig. 5). The input side is driven by a torque-controlled actuator at a 1 kHz loop. Each cable end is attached to a pretension-adjustable fixture; the initial pretension is set by screw adjustment and measured by inline load cells at both ends.

For model evaluation, the output pulley is coupled to a second torque-controlled backdrivable actuator, resulting in a symmetric dual-actuator setup. This configuration allows (i) repeatable torque excitation on the input side and (ii) programmable passive output dynamics on the driven side, which together serve as the basis for stiffness fitting, hysteresis characterization, and output-torque prediction in the subsequent sections. Specifically, the input actuator tracks a commanded torque trajectory $\tau_{in} = \tau_{des}$, while the output actuator emulates a linear passive environment via

$$\tau_{out} = b_{out}\dot{q}_{out} + k_{out}q_{out}, \quad (22)$$

with respect to the initial equilibrium position.

We record τ_{in} , τ_{out} , and the pulley coordinates (q_{in}, q_{out}) . In the present experiments, an NDI motion-capture system is used to reconstruct the sheath centerline as a geometric input for model validation. The reconstructed 2D routing is fitted by a planar spline and re-sampled at uniform arc length to obtain the curvature profile $\kappa(s)$ in magnitude [25], where $s \in [0, L]$ denotes the physical arc-length coordinate and L is the total routing length. The accumulated bending angle is computed as $\theta = \int_0^L \kappa(s) ds$. Routing conditions are grouped by θ_j (Fig. 4) by adjusting the distance between the two actuators. These bending groups span a broad range from strongly bent to near-flat routings; importantly, the validation does not assume constant curvature, since each group is represented by its measured (potentially non-uniform) $\kappa(s)$, including multi-bend routings with localized high-curvature regions. This provides a practical check of how well the model generalizes to non-uniform and multi-bend routings. The collected datasets (torques, displacements, routing, and pretension) are used to parameterize the model and evaluate its qualitative trends and predictive accuracy; further hardware details are provided in [25].

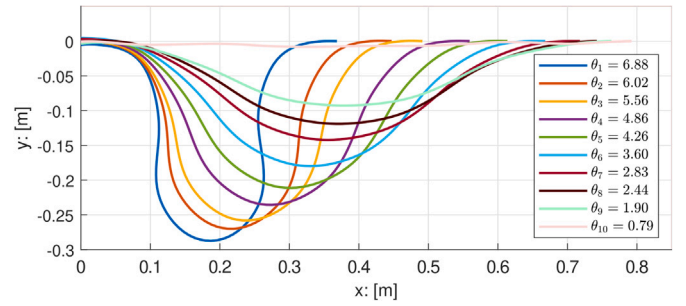


Fig. 4. Recorded cable routing path configuration of θ_j with $j = 1 \dots 10$.

4.2. Model setting

The proposed transmission model is evaluated in simulation by directly incorporating measured routing and pretension into the distributed dynamics in (7). The objective of this section is to define a consistent and reproducible parameter set for all subsequent experiments, rather than to perform parameter identification.

The model is implemented in Simulink (MathWorks Inc.) and integrated using a variable-step solver (ODE45). We used measured $\kappa(s)$ from Section 4.1 as input. The uniform segment stiffness k is identified once from torque-deflection measurements and held fixed across all conditions; its estimation is detailed in Section 4.3.1.

Table 3 summarizes the parameters used in this section. The quantities marked as *Recorded* are obtained directly from the experiment, while the remaining parameters are either set by design (e.g., pulley radii) or chosen to represent passive motor-environment dynamics on the output side. The friction coefficient μ is selected as $\mu = 0.052$, consistent with our previous experimental identification [25], and is kept fixed across all routing and pretension conditions to isolate geometric effects. Output-side stiffness k_{out} and damping b_{out} are varied only when explicitly studying environmental dynamics (Section 4.3.4); otherwise, they remain constant.

All simulations are performed in millimeter-based units to avoid numerical scaling issues associated with small cable displacements. Unless stated otherwise, the same parameter set is used across all discretization levels N , routing configurations θ_j , and excitation profiles. This ensures that observed variations in transmission behavior can be attributed to geometry, pretension, and environment dynamics rather than parameter retuning.

4.3. Transmission factor variation and characteristics analysis

This subsection characterizes the *transmission behavior* induced by the distributed friction and elasticity in the dual tendon-sheath system, including (i) time-domain hysteresis/backlash under torque excitation and (ii) the associated input-output torque/deflection transmissibility trends. Experiments and simulations are conducted under controlled variations of each factor while keeping all others nominally fixed. In all cases, the input actuator is driven by smooth torque profiles with a peak amplitude of 10 Nm, implemented either as a single sinusoid or as a superposition of multiple sinusoids. The same excitation is applied in experiment and simulation to ensure consistent comparison. The results are presented to highlight consistent transmission characteristics across routing, pretension, and load conditions, together with quantitative statistics where relevant.

4.3.1. Effective transmission stiffness

Across all investigated routing, pretension, and output dynamics conditions, the transmission exhibits a well-defined effective torsional stiffness. This stiffness is estimated from the steady-state slope of the hysteresis loop between the input torque τ_{in} and the relative angular

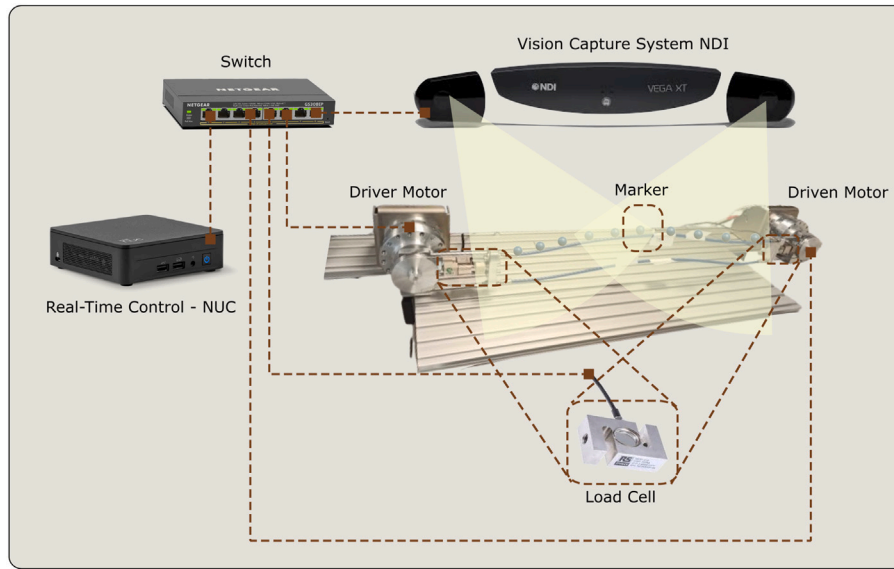


Fig. 5. Overview of the proposed testbed. To evaluate the proposed model, both actuators are controlled in torque mode and read the states in real-time.

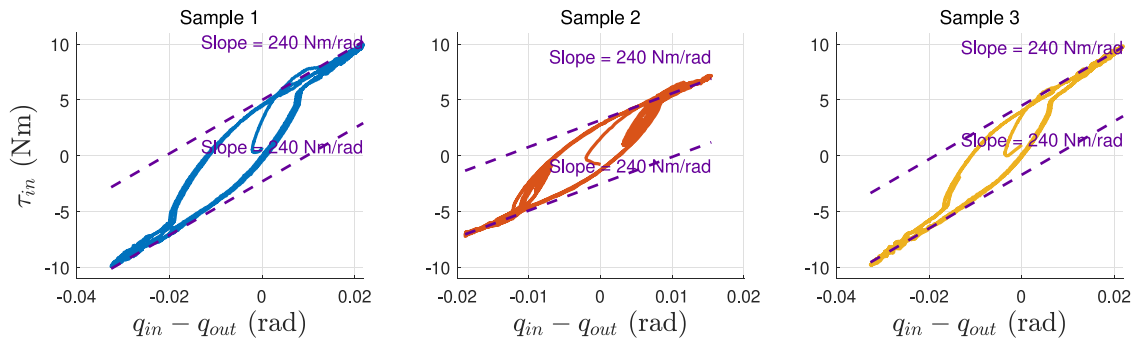


Fig. 6. Experimental results: The effective torsional stiffness between input torque and deflection. Three representative samples, obtained by commanding τ_{des} as either a simple sinusoidal function or a superposition of sinusoids and conducting experiments under varied transmission-factor conditions, show that the stiffness converges to 240Nm/rad, remaining invariant to transmission effects.

deflection ($q_{in} - q_{out}$), which captures the asymptotic compliance of the transmission under cyclic excitation. As shown in Fig. 6, the estimated stiffness consistently converges to approximately 240Nm/rad and remains invariant to the transmission factors considered in this study.

This invariance indicates that the effective stiffness is governed by a global elastic compliance of the transmission, which is examined in detail through the distributed stiffness analysis in Section 4.3.5. Accordingly, stiffness is treated as a global transmission characteristic and serves as a fixed baseline for the subsequent analysis of nonlinear effects.

4.3.2. Effect of pretensions

Here, the varied initial pretension is applied via the adjustable fixtures with screwing extent, with all other parameters kept nominally constant. The pretension applied to the curved surface of the bent sheath acts as a normal load, that directly contributes to friction force. Fig. 7(a) (experiment) and (b) (model) show that different levels of pretension result in varying levels of friction, as indicated by the intercepts at $\tau_{in} = 0$ or height of the backlash. For example, the 220 N group exhibits higher friction. Fig. 7(c) further highlights these differences, where pretension groups display distinct tension ranges. However, the tension transmission constant $e^{\pm\mu\theta}$ [10] remains unaffected by pretension level through groups shown in Fig. 7(c), which

implies that the pretension directly contributes to torque domain of the friction instead of tension transmission contained friction.

4.3.3. Effect of shapes

In the experiments, the distance between the two actuators was adjusted to vary the bending shape while keeping other settings nominally identical. Due to tendon–sheath clearance and distributed dry friction, changing the routing shape inevitably perturbs the actual pretension, making it difficult to maintain a strictly constant pretension across configurations (addressed later in Section 4.4). For the present qualitative analysis, the pretension measured by the inline load cell is treated as approximately constant under a simplifying assumption.

The cable shape determines how the applied pretension is converted into normal force along the sheath, thereby influencing the friction magnitude. As shown in Fig. 7(d) (experiment) and (e) (model), increased bending leads to higher friction, while the measured pretension levels remain nominally comparable across configurations (Fig. 7(f)).

The slope of the forward-motion branch in the torque hysteresis reflects the effective transmission ratio between input and output torque. When the slope is close to unity, τ_{in} is transmitted with minimal loss, as the tension increase in one cable is balanced by the release of the opposing cable at the same location (see also Section 4.3.5). In contrast, slopes exceeding unity are indicative of the onset of stiction, revealing

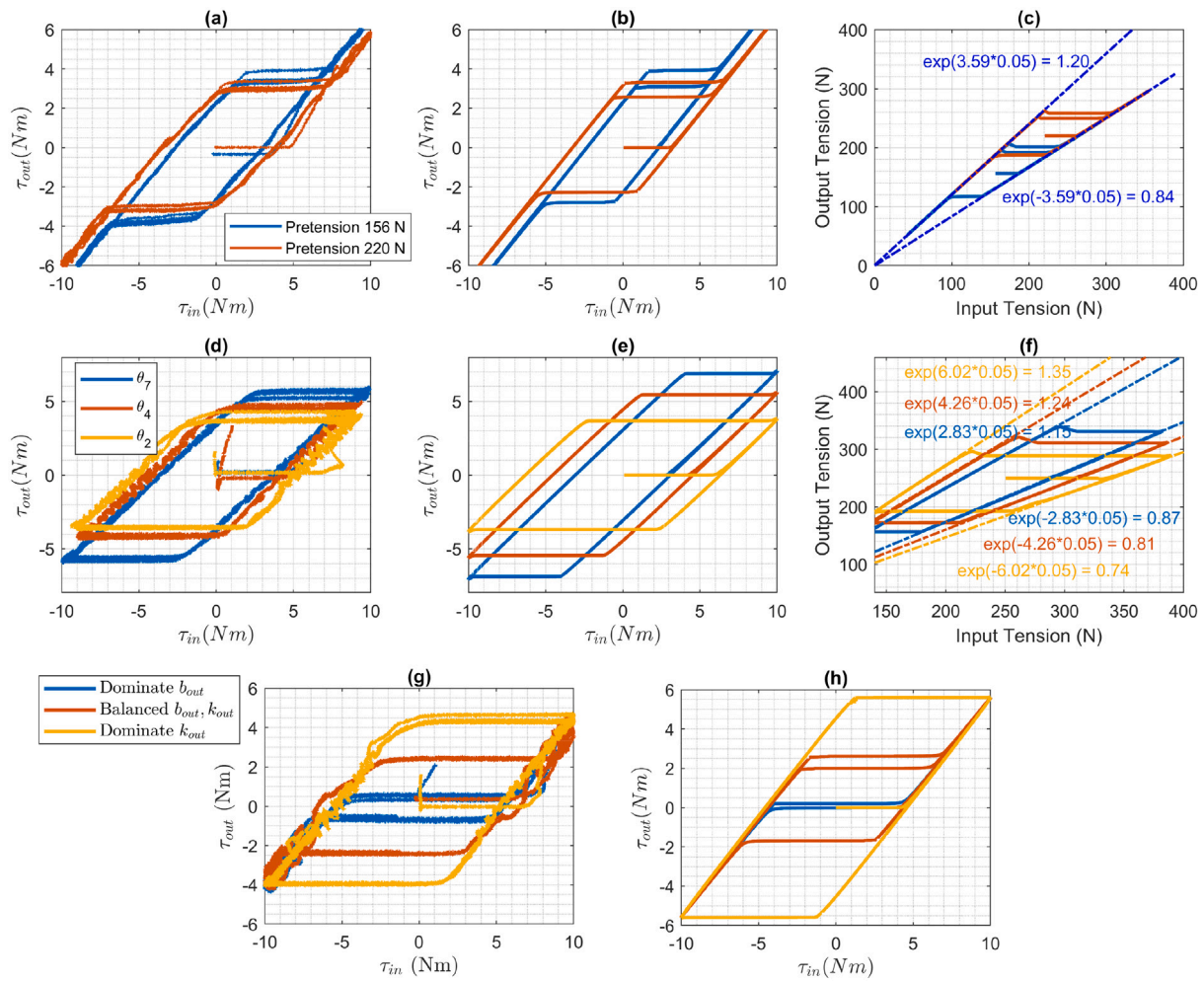


Fig. 7. Model and experimental results: the input–output torque and tension relationships under varying pretension, shape and load dynamics conditions. (a)–(b): Hysteresis loops of input–output torques dependent on different pretension level from experiment and proposed model, respectively. (c): Tension transmission slope fitted by exponential decay for pull and push phases from proposed model. (d)–(e): Hysteresis loop under different curvature configurations θ , from experiment and proposed model, respectively. (f): Comparison of tension transmission slopes with fitted exponential factors under multiple routing conditions from proposed model. (g)–(h): Hysteresis shape depends on environmental dynamics shape.

that tension is no longer uniformly balanced along the transmission path.

This effect is further illustrated by the tension transmission results in Fig. 7(f), where the forward and backward branches follow the theoretical efficiency factors $e^{-\mu\theta}$ (pulling) and $e^{\mu\theta}$ (pushing). These observations confirm that routing shape primarily influences friction through curvature-induced normal forces, independently of the nominal pretension level.

4.3.4. Effect of output dynamics

Transmission dynamics can be influenced by output environment [26]. The output dynamics are simplified into linear damping and spring forces composition in proposed model, presenting a passive environment, denoted by k_{out} and b_{out} (i.e., potential and dissipative load). For example, gravity acts as a potential load that seeks to return the system to its resting position, contributing to a certain backlash level when stiction stores potential force. Dissipative forces, in contrast, do not maintain backlash saturation since they dissipate energy and does not resist system to resting state. Experiment and model in Figs. 7(g) and (h) show that environments dominated by potential loads store more of the received torque, maintaining higher backlash levels.

4.3.5. Distributed stiffness and friction

Beyond the isolated effects of bending, pretension, and output dynamics, cable transmission must be regarded as a spatially distributed process rather than a lumped spring. Compliance arises jointly from the elastic tendon and its flexible sheath, which act in series to distribute displacement and tension along the cable. The interaction of this distributed stiffness with local friction governs the overall torque transmission characteristics.

All experiments in this section use smooth 10 Nm peak input torques. For Figs. 8(a,b,e,f), a single sinusoid is applied experimentally. Figs. 8(c,d) show proposed model with a two-term Fourier input to highlight tension and displacement propagation. Figs. 8(e,f) reuse the experimental dataset from Figs. 8(a,b) under different variables.

The effective torsional stiffness is benchmarked against a nominal $K_q \approx 382 \text{ Nm/rad}$.¹ Measured and simulated values are consistently lower (Figs. 6, 8(a,b)), indicating additional compliance from the sheath; creep under sustained load may further reduce tendon stiffness.

Fig. 8(a) shows that the proposed model reproduces the hysteresis loop of torque vs. deflection imposed by the environment. The effective

¹ Using $E = 210 \text{ GPa}$, $A = 3.14 \text{ mm}^2$, $r = 1 \text{ mm}$, $L = 1379 \text{ mm}$, the torsional stiffness of one cable is $K_{q,1} = \frac{EAr^2}{L}$. For two identical cables in series, $K_q = \frac{K_{q,1}K_{q,2}}{K_{q,1}+K_{q,2}}$.

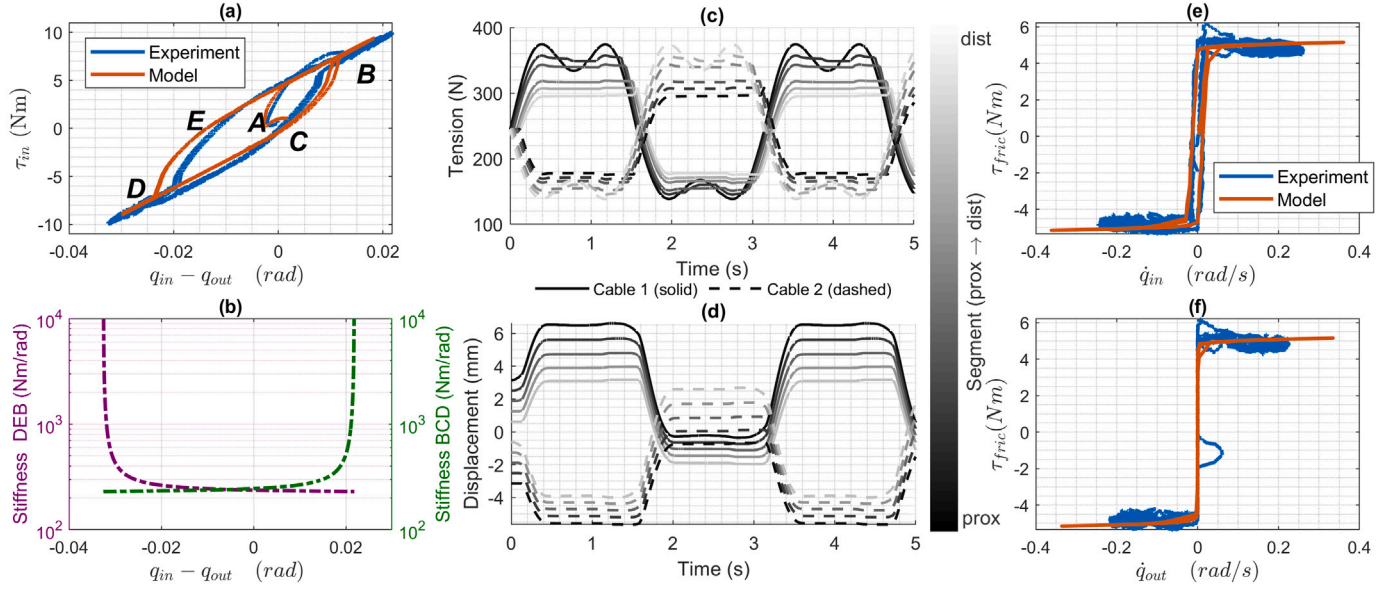


Fig. 8. Model and experimental results: Physical insight of distributed features. (a) Distributed transmission modeling reproduces hysteric stiffness loop. (b) Reciprocal stiffness transition of forward (AB or DEB) and back (BCD) motion showing in log plot. (c) Distributed tension profiles in two cables from proximal to distal joints over time evolution, illustrating propagation and local saturation. (d) Displacement profiles distributed in two cables from proximal to distal joints, showing shape evolution under cyclic motion correspondent to (c). (e) Identified friction torque versus input angular velocity, comparing experiment and model prediction. (f) Identified friction torque versus output angular velocity, comparing experiment and model prediction. The augmented narrow show the cold-start sticky friction peak.

stiffness, taken as the slope of τ_{in} vs. $(q_{in} - q_{out})$, is motion-dependent: forward motion (A→B) engages only part of the cable, giving a steep initial slope that flattens as more segments engage; backward motion (B→C→D) mirrors this (D→E→B), yielding reciprocal stiffness (Fig. 8(b)). Stiffness is undefined across zero-deflection crossings.²

Tension propagation is non-uniform (Fig. 8(c)): proximal tension damps toward the distal joint, attenuating high-frequency content. Symmetric propagation occurs in both cables, with proximal segments responding more and saturating earlier. Displacement profiles (Fig. 8(d)) show deformation mainly during non-stiction phases, with saturation zones aligning qualitatively with τ_{out} in Fig. 1(b). These distributed effects complicate friction modeling. Using input velocity as the friction state yields a hysteresis-like loop (Fig. 8(e)), reflecting uncollocated tension and displacement. Using output velocity produces a more Coulomb-like curve (Fig. 8(f)), indicating less hysteresis from the joint end that is useful for friction estimation in control. This also provides physical insight later examined in the sensitivity analysis, particularly the interplay of distributed compliance and friction under model discretization.

4.4. Model prediction

This section evaluates the proposed model's prediction capability by simulating output torque based on experimental input torque trajectories, under various conditions of bending and environment dynamics.

4.4.1. Prediction under discretized pretension

In practice, pretension is measured independently at the input and output sides via inline load cells. In this work, we adopt a symmetric approximation by assigning the nominal boundary pretension as the average of the two measurements, which simplifies the exposition without loss of generality. The proposed formulation does not rely on

symmetry and can accommodate asymmetric boundary pretensions by treating the two contributions independently.

Accordingly, the nominal boundary pretension is assigned as

$$T_0(\bar{s} = 0) = T_0(\bar{s} = 1) = \frac{1}{4}(T_{lc,in} + T_{lc,out}),$$

where $\bar{s} \in [0, 1]$ denotes the normalized arc-length coordinate, and we write the curvature integral in normalized form with $\kappa(\cdot)$ evaluated along the corresponding physical arc length. Since the tension propagation along curved sliding surface is followed by,

$$\begin{aligned} T(\bar{s}) &= T_0(\bar{s} = 0)e^{-\mu \int_0^{\bar{s}} L\kappa(L\sigma) d\sigma} \\ &= T_0(\bar{s} = 1)e^{-\mu \int_1^{1-\bar{s}} L\kappa(L\sigma) d\sigma}, \end{aligned} \quad (23)$$

it is possible to find the minimum pretension $T_0(\bar{s}_{min})$ at its location \bar{s}_{min} by solving

$$e^{-\mu \int_0^{\bar{s}_{min}} L\kappa(L\sigma) d\sigma} = e^{-\mu \int_1^{1-\bar{s}_{min}} L\kappa(L\sigma) d\sigma}. \quad (24)$$

Here, $T_0(\bar{s} = 0)$ denotes the proximal pretension, and $\kappa(L\sigma)$ denotes the physical curvature evaluated at the arc-length location corresponding to the normalized coordinate $\sigma \in [0, 1]$. For discrete implementations, the segment where the cumulative attenuation from both ends is balanced defines the location of minimum pretension \bar{s}_{min} . Fig. 9(a,b) visualizes the curvature-induced pretension distribution along the cable, illustrating the emergence of a minimum-pretension region under bending and its contraction as curvature increases.

To illustrate the discretization sensitivity of the distributed pretension representation, we first examine two extremity cases: $N = 1$ and $N = 10$, using fixed shape, pretension, and output dynamics. The $N = 1$ case uses a single-sine input, while $N = 10$ uses a three-term superposed sine input; in both, the remaining parameters are identical. The results show that for the more bent group, $N = 10$ yields accurate predictions, whereas $N = 1$ deviates substantially. For flatter shapes, both cases perform comparably, suggesting that weak curvature produces nearly uniform pretension distributions, making the prediction less sensitive to discretization. Notably, in the near-flat routing case of Fig. 9(d,f), small ripples appear in $\tau_{out,sim}$ around motion onset (e.g., at $t \approx 6, 10, 14$ s). These ripples persist across discretizations

² Torque-to-deflection ratios across zero crossings are not meaningful.

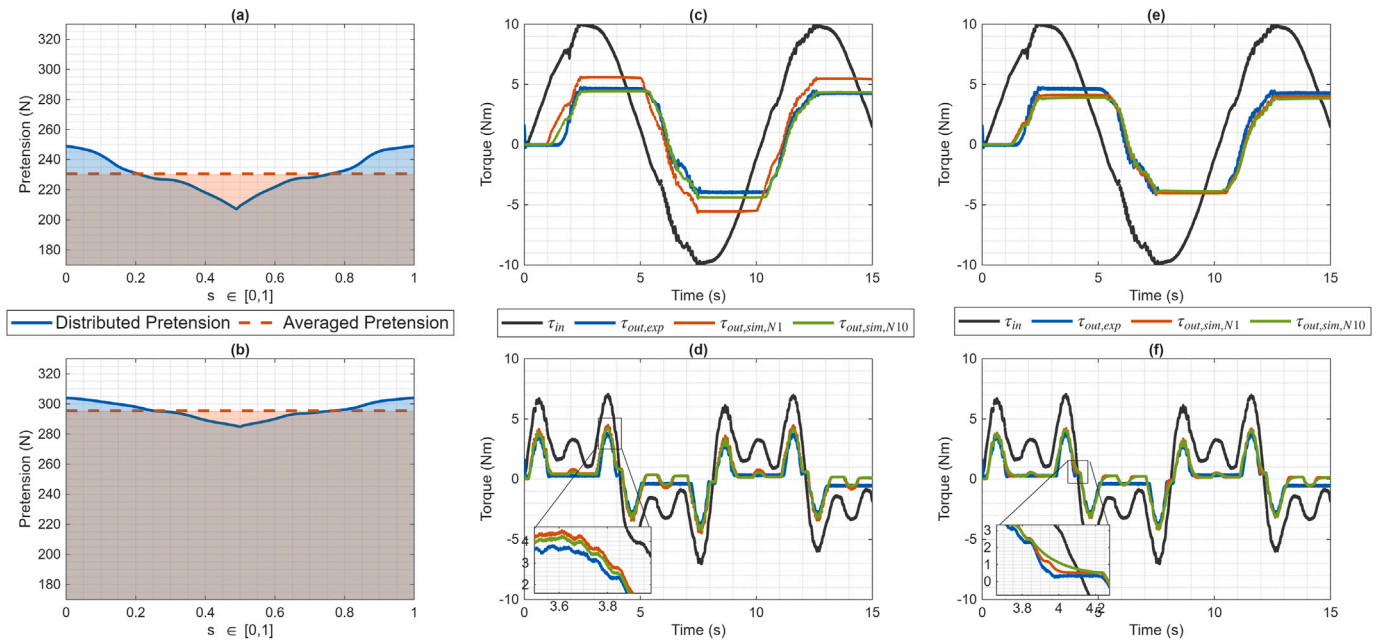


Fig. 9. Model and experimental results: model prediction validation on two demonstrative cases with extreme conditions. The first row shows results on simple sinusoidal input trajectory, potential load, most bending shape θ_1 . While second row shows complex input trajectory, damping dominated load, highly flat bending shape θ_8 . (a–b) show the two discussed pretension estimate visualization. (c–d) show the prediction result with respect to the distributed pretension estimate. (c) RMSE = [1.2132, 0.3839] Nm for both $N=1$ and 10, (d) RMSE = [0.5108, 0.4101] Nm for both $N=1$ and 10. (e–f) show the prediction result with respect to the average pretension estimate. (e) RMSE = [0.4406, 0.5699], Nm for both $N=1$ and 10, (f) RMSE = [0.3989, 0.3944] Nm for both $N=1$ and 10.

N , suggesting that the mismatch is dominated by history-dependent pre-sliding/stiction effects associated with the unobserved internal pretension/friction distribution, rather than by spatial discretization of the routing geometry.

To complete the validation of the model prediction, a sensitivity analysis was conducted across all bending groups and discretization levels (Fig. 10). The model maintains low root mean square error (RMSE) when more than 4–5 segments are used, but steeply bent shapes (θ_1 – θ_5) suffer from large errors under coarse discretization. An exception is θ_{10} , the flattest group, which exhibits unexpectedly high RMSE — likely due to greater sensitivity to visual marker placement in flat configurations, causing overfitting in spline-based reconstruction and mismatch in the modeled shape. These results indicate that under highly non-uniform curvature, coarse spatial discretization cannot capture local curvature heterogeneity, leading to pronounced sensitivity in torque prediction. This breakdown, evident from the heightened sensitivity in Fig. 10, motivates the development of the averaged pretension estimation in Section 4.4.2, which reduces reliance on fine discretization while preserving key transmission dynamics.

The above results indicate that assuming constant pretension, as commonly adopted in [12,16], can lead to inaccurate predictions for thick and frictionally adhesive tendon–sheath systems, unlike lumped models that may require recalibration for different shapes [21]. Moreover, the proposed approach eliminates reliance on threshold-based detection and enables smoother transitions compared to analytical transmission models [12,25]. As seen from the varying backlash saturation profiles by consistently quantifying the environment dynamics using k_{out}/b_{out} ratio, compared with the previous model, the explicit transmission state and the double-sided pretension approximation lead to more stable hysteresis and more robust predictions.

4.4.2. Averaged pretension estimation — model order reduction (MoR)

To mitigate the sensitivity of the distributed pretension estimation to coarse spatial discretization, we introduce an averaged pretension formulation that replaces the non-uniform pretension field with

an equivalent uniform representation preserving the overall frictional transmission effect. The averaged pretension is constructed such that the total frictional torque predicted by the distributed model under steady sliding is preserved as

$$T_{0,eq} = T_0(\bar{s} = 0) \left(e^{-\mu \int_0^{\bar{s}_{min}} L\kappa(L\sigma) d\sigma} + e^{-\mu \int_1^{1-\bar{s}_{min}} L\kappa(L\sigma) d\sigma} \right). \quad (25)$$

Here, \bar{s}_{min} is the balanced-attenuation location defined in (24). Fig. 9(a,b) illustrates the resulting equivalent uniform pretension used in the reduced model.

With this formulation, torque predictions become consistent across different discretization levels, as shown in Fig. 9(e,f), even for small numbers of segments N . This confirms that the averaged pretension captures the dominant frictional effect of the distributed transmission without requiring fine spatial resolution.

Beyond discretization robustness, the reduced analytical model in (20) is further evaluated through comparison with existing analytical transmission models, namely Wu’s model [12] and our previous formulation [25]. Wu’s model assumes constant curvature and uniform pretension, yielding a compact analytical mapping under idealized routing conditions. Our previous model extends this formulation to non-constant curvature by introducing a single-sided pretension representation. In contrast, the present work adopts a double-sided pretension representation consistent with practical pretensioning procedures and derives the analytical transmission law directly from the distributed model via the averaged pretension reduction.

For a fair comparison, both of our models use the same friction coefficient. Wu’s model parameters are identified independently via a least-squares fit. The remaining parameters are identified using a single reference trajectory at an intermediate bending configuration (θ_5). The results in Fig. 11(a,b) show that neglecting explicit pretension distribution results in larger prediction errors for thick, highly adhesive tendon–sheath systems. Both specification-based models (our previous work and the present formulation) exhibit consistent sensitivity trends as the routing becomes flatter, in agreement with the

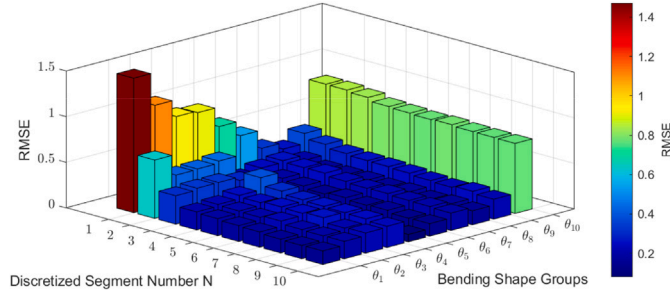


Fig. 10. Model results: sensitivity analysis plot with respect all bending shape and discretizations for model prediction. Z-axis shows the RMSE in Nm between predicted and experimental output torques.

distributed-model analysis, whereas Wu’s model shows limited generalization across bending configurations.

Under damping-dominated output conditions, all reduced models experience increased prediction error, as reflected by the RMSE trends. However, Wu’s model and our previous formulation retain threshold-based gating mechanisms that introduce abrupt hysteresis transitions. In contrast, the present model preserves an independent virtual transmission state inherited from the distributed formulation, resulting in smooth hysteresis evolution and continuous motion transitions, as highlighted in the zoomed regions of Fig. 11(c,d) and the corresponding τ_{in} - τ_{out} loops in Fig. 11(e,f). Overall, the proposed averaged-pretension model demonstrates improved robustness with respect to coupled bending and pretension variations while maintaining a physically consistent analytical structure.

4.5. Application use case: Friction compensation

This section demonstrates the practical benefit of the proposed model for improving interaction transparency as application of use cases. A key challenge is that the proposed distributed transmission model (7) as well the reduced analytical model (20) rely on internal transmission states that are not directly measurable, making full state-based control impractical. To demonstrate practical usability under limited sensing, we adopt a strategy inspired by [21], integrating the reduced analytical model (Section 3.3) and its averaged pretension estimate (Section 4.4.2) into a Linear Disturbance Observer (LDO) framework. The LDO is adapted to account for cable-elasticity-induced torque degradation, controlling τ_{in} with respect to the desired $\tau_{in,des}$ motor command τ_m , and enabling partial feedforward friction compensation as a direct validation of the analytical transmission model.

The nominal plant from τ_m to τ_{in} is

$$P_{m,n}(s) = \frac{\tau_{in}(s)}{\tau_m(s)} = \frac{K_c}{J_m s^2 + B_m s + K_c}, \quad (26)$$

with motor-side inertia J_m , damping B_m , and cable stiffness K_c taking the steady state value from Fig. 6.

The LDO consists of: nominal dynamics $P_{m,n}(s)$, observer filter $Q_m(s)$ (designed as a second order Butterworth filter), and PD feedback $C(s) = K_p + K_d s$. The disturbance estimate is

$$\hat{d}(s) = -Q_m(s) \left[P_{m,n}^{-1}(s) \tau_{in}(s) - \tau_m(s) \right], \quad (27)$$

which lumps motor-side friction, unmodeled stiffness effects, and rapid torque variations induced by adhesive stick-slip phenomena. The motor control torque is composed with compensation terms,

$$\tau_m = C(s) (\tau_{in,des} - \tau_{in}) + \tau_{in,des} + \hat{d}(s) + \hat{\tau}_{f,c}(s), \quad (28)$$

where $\hat{\tau}_{f,c}(s)$ is the reduced-model friction feedforward as shown in (21), evaluated using \dot{q}_{out} as a measurable velocity signal in place of the unobservable internal transmission state \dot{q} . The complete LDO implementation follows [21].

4.5.1. Control structure and experimental protocol

Fig. 12 shows the control loop used for validating the reduced analytical transmission model. The desired output torque is set to the gravity term $\tau_{out,des} = \hat{\tau}_g(q_{out})$, computed from the link-IMU measurement of q_{out} . The same IMU also provides \dot{q}_{out} for the model-based friction feedforward $\hat{\tau}_{f,c}$:

A low-level torque controller (PID or LDO) commands the motor torque τ_m to track the desired output torque $\tau_{out,des}$. $\hat{\tau}_{f,c}$ is determined by the inline load cell $T_{0,eq}$ and vision-based shape sensing θ_j .

For interactive experiment, the driven actuator is replaced by a rigid aluminum link (500 × 20 × 20 mm) with a 500 g tip mass. The link is instrumented with: (i) a Magtrol TM307 inline torque sensor and Kübler encoder (monitoring only), (ii) an MTi-630 AHR IMU (400 Hz, used for control), and (iii) a Mini40 6-axis F/T sensor with a 3D-printed handle (monitoring only). The link is manually backdriven under two conditions — without and with $\hat{\tau}_{f,c}$ — using an asymmetric cable shape. Only gravity compensation is applied so that the user perceives the link’s natural passive dynamics, enabling direct comparison of interactive transparency. Overall, the low-level torque loop runs at 1 kHz, with the model-based compensator $\hat{\tau}_{f,c}$ updated at 400 Hz by \dot{q}_{out} . To contextualize the excitation regime, we report a characteristic frequency scale associated with the torque transmission using the identified equivalent stiffness and the effective motor inertia. With $J_m \approx 0.73 \text{ kg m}^2$ and $k_c \approx 240\text{--}280 \text{ N m/rad}$, the corresponding natural-frequency is $f_n = \frac{1}{2\pi} \sqrt{k_c/J_m} \approx 2.9\text{--}3.1 \text{ Hz}$ when the output is assumed stiff. In practice, finite output impedance (load compliance/inertia/damping) reduces the achievable torque-transmission frequency range in interaction, and the experiments in this section therefore use low-frequency excitations consistent with this regime [31].

4.5.2. Results

Fig. 13 summarizes the measured interaction torques under different conditions:

- (a): No friction compensation; pronounced stick-slip and residual friction.
- (b,c): With friction feedforward under different motion speeds and bending conditions.

Without compensation, strong friction-induced hysteresis degrades interaction transparency. With compensation, the interaction torque magnitude is significantly reduced, indicating improved backdrivability. In slow back and forth motion (with high bending), the benefit is most visible. In fast motion, natural link impedance becomes more prominent, with LDO exhibiting improved tracking under fast motion due to its model-informed structure. Residual impedance persists near quasi-static reversals, highlighting the model’s inability to fully capture sticky friction and motivating future closed-loop friction observers.

Quantitatively, Fig. 13(d) shows mean absolute interaction torque, where the compensated cases reduce torque error to around 0.5–0.6 Nm, compared to the uncompensated baseline of 3.37 Nm. Also, LDO outperforms PID in fast motion due to better tracking of high-frequency components.

5. Discussion

This work builds upon prior studies that share related modeling perspectives but differ in several key aspects. Compared to Agrawal et al. [16], we extend from a static, scalar-valued tension formulation to a dynamic, discretized framework that explicitly resolves the interaction between distributed pretension and torque/tension propagation. Unlike position-conditioned or lumped models, our formulation reveals how local stiffness and friction jointly shape the global transmission behavior.

The proposed model also reproduces known trends, namely, the influence of stiffness and pretension reserves on hysteresis shape and

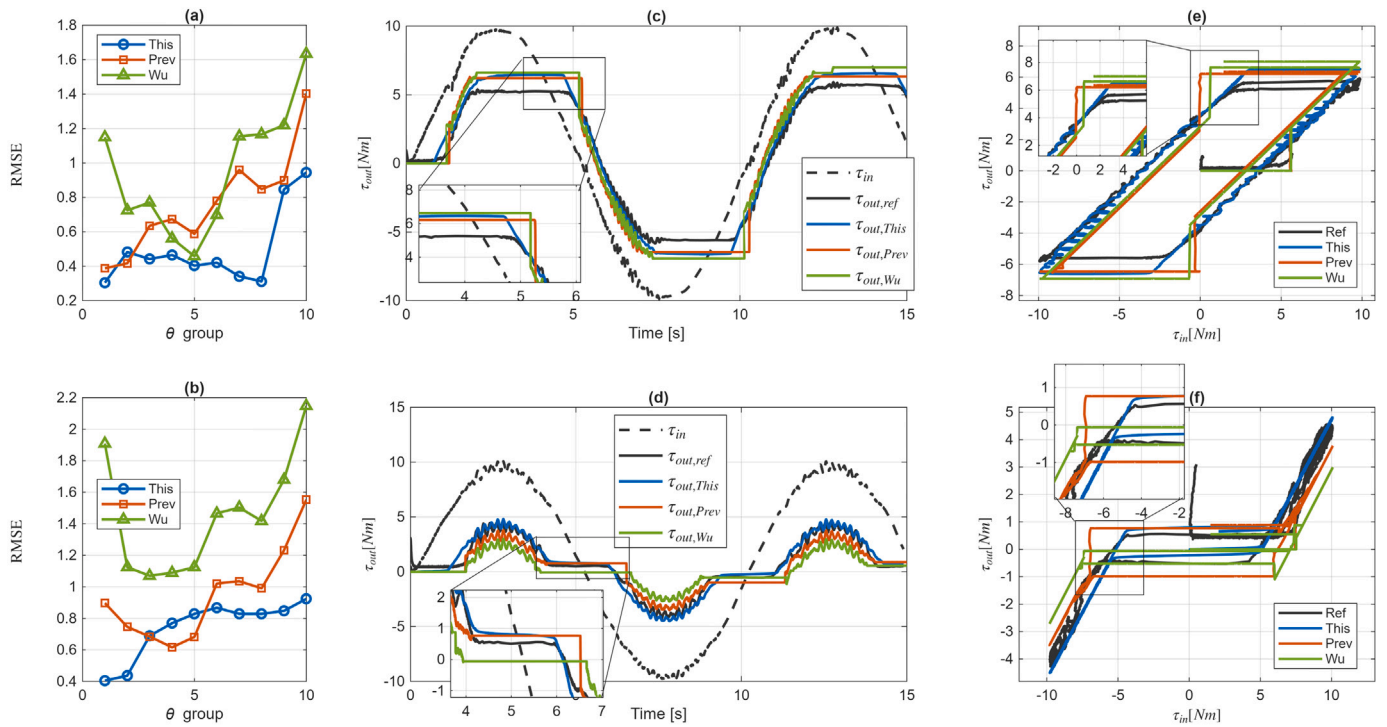


Fig. 11. Comparison between analytical models. To be compared are the models in **This** work, our previous (**Prev**) work [25] and **Wu**'s work [12]. (a–b) present benchmarking of all models through all bending groups and divided into two output dynamics groups, i.e. (a)-dominated stiffness, (b)-dominated damping. (c,e) present results of flat bending θ_1 with stiff output. (d,f) present result of large bending θ_2 with damped outputs. In (c), the RMSE results are given by [0.3416, 0.9600, 1.1549] Nm, and in (d), the RMSE results are with [0.4366, 0.7461, 1.1245] Nm.

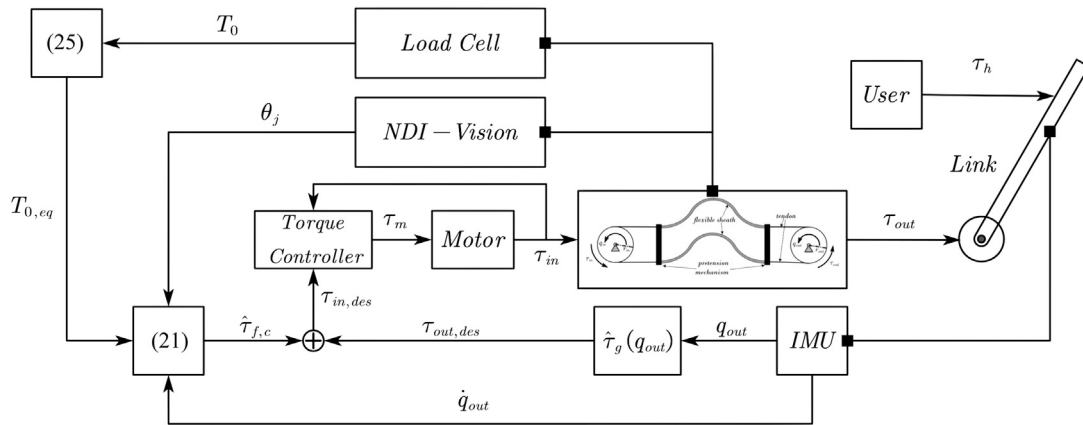


Fig. 12. Control configuration for interactive use-case in Friction Compensation. $\hat{\tau}_g(q_{out})$ indicates the gravity model.

torque linearity which are consistent with prior empirical observations [16,18]. As these effects have been extensively reported, the corresponding results are omitted here for conciseness. In contrast to the work by Buchanan et al. [26], which incorporates pretension-related effects via embedded sensing and threshold-based compensation, our approach enables direct quantitative prediction by exploiting boundary load measurements at both cable ends, without the need for internal sensing or threshold tuning.

Furthermore, we emphasize that our model adopts a fixed friction coefficient, and does not rely on additional identification or data fitting involving $\mu\theta$ combinations, as commonly used in other works. This deliberate simplification highlights the model's predictive capacity grounded in physical parameterization, rather than overfitting. In this

sense, the averaged-pretension formulation should be interpreted as a model reduction that preserves dominant transmission effects, rather than as an empirical fitting construct.

Although the model was validated in MATLAB/Simulink without real-time optimization, the computational efficiency has not been the primary goal of this study. Future implementations may explore tailored solvers or model reduction techniques for embedded or online applications.

A key limitation of the proposed model lies in its inability to capture localized stiction peaks in the pre-sliding regime, especially around motion onset after a rest phase. In practice, the pretension is often imperfectly distributed, especially when high pretension is applied to ensure transmission robustness. This can lead to an imbalance, with

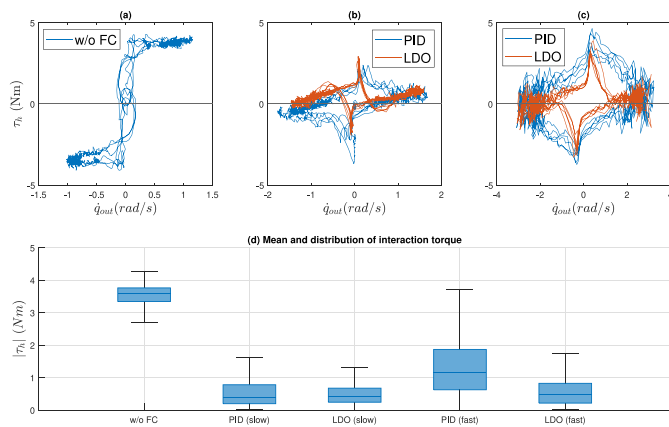


Fig. 13. Experimental results: Measured interaction torque τ_h . (a) Without compensation: strong stick-slip and residual impedance. (b) With compensation under slow motion (high bending). (c) With compensation under fast motion (low bending). (d) Mean absolute torque values in boxplot: [3.370, 0.642, 0.498, 1.334, 0.663] Nm from left to right.

one cable carrying significantly more sticky friction than the other upon motion onset. As shown in Fig. 8(e,f), these peaks manifest prominently at motion initiation but dissipate quickly during repetitive back-and-forth movements as tension redistributes. When motion halts and restarts, the peaks re-emerge unpredictably. This limitation may also explain the residual ripples in Fig. 9(d,f): localized breakaway timing can depend on the unobserved distribution of stiction/friction reserves and pretension along the routing, which is difficult to predict locally without distributed internal sensing or additional distributed friction states.

Such spatially localized stick-slip effects arise from unobservable distributions of tension along the cable path. They are not captured by classic lumped friction models such as LuGre [32] or more advanced variants like Palli et al. [17], which represent friction via single internal states. These models fundamentally assume spatial homogeneity or implicitly collapse spatial effects into lumped internal states. Addressing this limitation would require either distributed sensing or real-time estimation of the pretension field [26], both of which remain open research problems.

In practical systems, cable routings are not necessarily planar. For general 3D layouts, prior work suggests that the same discretization framework can be extended by providing an arc-length-parameterized spatial (possibly including torsional effects) routing descriptor (e.g., a curvature magnitude profile along the centerline) so that segment-wise curvature measures can still be discretized and propagated through the model [33]. While additional validation is required for such 3D cases, the proposed transmission model treats the cable routing as a prescribed geometric constraint, i.e., the centerline shape (and the associated curvature profile) is provided as an input to the model. As a result, the formulation captures axial transmission effects dominated by curvature-induced normal loading and frictional loss, while it does not introduce additional rod/beam degrees of freedom to model bending/torsional deformation dynamics of the sheath or tendon. This assumption is appropriate when the routing is mechanically constrained by the device structure (or varies slowly relative to the actuation bandwidth); if routing deformation under load becomes significant, coupling the present transmission model with a rod-based shape estimator is a natural extension [34]. Accordingly, the formulation mainly depends on curvature-dependent normal loading and frictional loss rather than on an exact local reconstruction of the entire centerline. We nevertheless acknowledge that optical tracking can be infeasible in embedded/occluded scenarios; in such cases, the required

curvature descriptors can be obtained from design geometry/calibration or from model-based shape reconstruction [35] potentially combined with sparse instrumentation [36], since a bending-stiff sheath under known boundary/guide constraints is well-approximated by a quasi-static (energy-minimizing) configuration [34].

Another open issue concerns the possible contribution of distributed viscous damping at higher motion speeds. While the reduced-order model retains a small lumped damping term f_b to account for unmodeled dynamics, its physical basis may include shear drag and internal sliding losses between tendon and sheath. These effects are negligible in the low-speed regime considered here but may become significant under fast or rapidly reversing motion, where a velocity-dependent hysteresis component may emerge. This behavior was not isolated in our study due to the limited velocity range. Future work could investigate this by extending experiments to higher speeds and refining the model to distinguish between distributed viscous effects and other nonlinearities.

6. Conclusion and future work

This work presents a framework for modeling dual cable-driven transmissions with distributed elasticity, pretension, and friction. A discretized model captures shape- and configuration-dependent effects, while a reduced-order formulation enables tractable friction estimation for torque-level applications. The model reveals how cable shape, boundary constraints, and local friction collectively shape torque transmission. It consolidates prior observations such as pretension bias, elastic stretch, and velocity-sensitive hysteresis — into a single physically interpretable structure. We demonstrate how such model-based friction compensation as a feedforward term improves transparency during interaction, even under sensing and hardware constraints.

CRedit authorship contribution statement

Yu Li: Writing – original draft, Visualization, Validation, Software, Methodology, Formal analysis, Data curation, Conceptualization. **Hamid Sadeghian:** Writing – review & editing, Supervision, Project administration, Methodology, Formal analysis, Conceptualization. **Moein Forouhar:** Writing – review & editing, Methodology. **Abdeldjalil Naciri:** Writing – review & editing, Resources, Project administration. **Sami Haddadin:** Resources, Funding acquisition.

Declaration of competing interest

The authors declare that they have no known competing financial interests or personal relationships that could have appeared to influence the work reported in this paper.

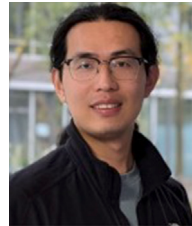
Data availability

Data will be made available on request.

References

- [1] Armanini C, Boyer F, Mathew AT, Duriez C, Renda F. Soft robots modeling: A structured overview. *IEEE Trans Robot* 2023;39(3):1728–48.
- [2] Dežman M, Asfour T, Ude A, Gams A. Mechanical design and friction modelling of a cable-driven upper-limb exoskeleton. *Mech Mach Theory* 2022;171:104746.
- [3] Toedtheide A, Chen X, Sadeghian H, Naciri A, Haddadin S. A force-sensitive exoskeleton for teleoperation: An application in elderly care robotics. In: 2023 IEEE international conference on robotics and automation. IEEE; 2023, p. 12624–30.
- [4] Gosselin C. Cable-driven parallel mechanisms: state of the art and perspectives. *Mech Eng Rev* 2014;1(1):DSM0004.
- [5] Zhang Z, Zhang G, Wang S, Shi C. Hysteresis modeling and compensation for tendon-sheath mechanisms in robot-assisted endoscopic surgery based on the modified Bouc-Wen model with decoupled model parameters. *IEEE Trans Med Robot Bionics* 2023;5(2):218–29.

- [6] Dittli J, Hofmann UA, Bützer T, Smit G, Lambercy O, Gassert R. Remote actuation systems for fully wearable assistive devices: requirements, selection, and optimization for out-of-the-lab application of a hand exoskeleton. *Front Robot AI* 2021;7:596185.
- [7] Kong K, Bae J, Tomizuka M. Control of rotary series elastic actuator for ideal force-mode actuation in human-robot interaction applications. *IEEE/ASME Trans Mechatronics* 2009;14(1):105–18.
- [8] Dupont PE. Avoiding stick-slip through PD control. *IEEE Trans Autom Control* 1994;39(5):1094–7.
- [9] Pratt J, Krupp B, Morse C. Series elastic actuators for high fidelity force control. *Ind Robot: Int J* 2002;29(3):234–41.
- [10] Chen L, Wang X. Modeling of the tendon-sheath actuation system. In: 2012 19th international conference on mechatronics and machine vision in practice (m2VIP). IEEE; 2012, p. 489–94.
- [11] Zhang Q, Wang X, Tian M, Shen X, Wu Q. Modeling of novel compound tendon-sheath artificial muscle inspired by hill muscle model. *IEEE Trans Ind Electron* 2017;65(8):6372–81.
- [12] Wu Q, Wang X, Chen L, Du F. Transmission model and compensation control of double-tendon-sheath actuation system. *IEEE Trans Ind Electron* 2014;62(3):1599–609.
- [13] Chen L, Wang X, Xu W. Inverse transmission model and compensation control of a single-tendon-sheath actuator. *IEEE Trans Ind Electron* 2013;61(3):1424–33.
- [14] Lu Y, Li H, Shi K, Lai J, Li Y, Zhang M, Song A. A comprehensive control method for tendon-sheath system using friction model-based angle estimation and feedforward-feedback control in time-varying configurations. *IEEE Trans Ind Electron* 2023;71(5):5166–75.
- [15] Amundsen DS, Trømborg JK, Thøgersen K, Katzav E, Malthé-Sørensen A, Scheibert J. Steady-state propagation speed of rupture fronts along one-dimensional frictional interfaces. *Phys Rev E* 2015;92(3):032406.
- [16] Agrawal V, Peine WJ, Yao B. Modeling of transmission characteristics across a cable-conduit system. *IEEE Trans Robot* 2010;26(5):914–24.
- [17] Palli G, Borghesan G, Melchiorri C. Modeling, identification, and control of tendon-based actuation systems. *IEEE Trans Robot* 2011;28(2):277–90.
- [18] Agrawal V, Yao B, Peine WJ. Modeling of viscoelastic cable-conduit actuation for MRI compatible systems. *J Dyn Syst Meas Control* 2013;135(5):051004.
- [19] Vossoughi R, Donath M. Robot Finger Stiffness Control in the Presence of Mechanical Nonlinearities. *J Dyn Syst Meas Control* 1988;110(3):236–45.
- [20] Sun Z, Wang Z, Phee SJ. Elongation modeling and compensation for the flexible tendon-sheath system. *IEEE/ASME Trans Mechatronics* 2013;19(4):1243–50.
- [21] Jung Y, Bae J. Torque control of a series elastic tendon-sheath actuation mechanism. *IEEE/ASME Trans Mechatronics* 2020;25(6):2915–26.
- [22] Kaneko M, Yamashita T, Tanie K. Basic considerations on transmission characteristics for tendon drive robots. In: Fifth international conference on advanced robotics' robots in unstructured environments. IEEE; 1991, p. 827–32.
- [23] Townsend W, Salisbury J. The effect of coulomb friction and stiction on force control. In: Proceedings. 1987 IEEE international conference on robotics and automation, vol. 4, IEEE; 1987, p. 883–9.
- [24] Johnstun CR, Smith CC. Modeling and design of a mechanical tendon actuation system. *J Dyn Syst Meas Control* 1992;114(2):253–61.
- [25] Pérez-Suay D, Li Y, Sadeghian H, Naciri A, Haddadin S. Torque transmission in double-tendon sheath driven actuators for application in exoskeletons. In: 2024 IEEE international conference on robotics and automation. IEEE; 2024, p. 4751–7.
- [26] Buchanan S, Sergi F. Dynamic modeling and state estimation of cable-conduit actuation during interaction with nonpassive environments. *IEEE/ASME Trans Mechatronics* 2020;26(5):2462–71.
- [27] Do T, Tjahjowidodo T, Lau MWS, Phee SJ. An investigation of friction-based tendon sheath model appropriate for control purposes. *Mech Syst Signal Process* 2014;42(1–2):97–114.
- [28] Shi Y, Gao Y, Lin W, He L, Mao X, Long Y, Dong W. Human-in-the-loop modeling and control of an upper limb exosuit with tendon-sheath actuation. *IEEE Robot Autom Lett* 2024.
- [29] Kang BB, Kim D, Choi H, Jeong U, Kim KB, Jo S, Cho K-J. Learning-based fingertip force estimation for soft wearable hand robot with tendon-sheath mechanism. *IEEE Robot Autom Lett* 2020;5(2):946–53.
- [30] Qian W, Liao J, Lu L, Ai L, Li M, Xiao X, Guo Z. CURER: A lightweight cable-driven compliant upper limb rehabilitation exoskeleton robot. *IEEE/ASME Trans Mechatronics* 2022;28(3):1730–41.
- [31] Calanca A, Fiorini P. A rationale for acceleration feedback in force control of series elastic actuators. *IEEE Trans Robot* 2018;34(1):48–61.
- [32] De Wit CC, Olsson H, Astrom KJ, Lischinsky P. A new model for control of systems with friction. *IEEE Trans Autom Control* 1995;40(3):419–25.
- [33] Wang Z, Sun Z, Phee SJ. Modeling tendon-sheath mechanism with flexible configurations for robot control. *Robotica* 2013;31(7):1131–42.
- [34] Bretl T, McCarthy Z. Quasi-static manipulation of a Kirchhoff elastic rod based on a geometric analysis of equilibrium configurations. *Int J Robot Res* 2014;33(1):48–68.
- [35] Orekhov AL, Ahronovich EZ, Simaan N. Lie group formulation and sensitivity analysis for shape sensing of variable curvature continuum robots with general string encoder routing. *IEEE Trans Robot* 2023;39(3):2308–24.
- [36] Rahman N, Deaton NJ, Sheng J, Cheng SS, Desai JP. Modular FBG bending sensor for continuum neurosurgical robot. *IEEE Robot Autom Lett* 2019;4(2):1424–30.



Yu Li received the B.Eng. degree in Mechanical Engineering from the Hanover University of Applied Sciences and Arts, Germany, in 2021, and the M.Sc. degree in Mechatronics and Robotics from the Technical University of Munich (TUM), Germany, in 2024. He is currently a Research Associate at the Munich Institute of Robotics and Machine Intelligence (MIRMI), TUM. His research interests include cable-driven robotic systems, nonlinear friction modeling, flexible joint dynamics, and control of surgical and human-interactive robots.



Hamid Sadeghian is a Group Leader at the Munich Institute of Robotics and Machine Intelligence (MIRMI), Technical University of Munich (TUM), Germany. His primary research interests lie in advanced robot control, particularly force and impedance control, as well as networked robotics. He currently serves as Principal Investigator of the European project FlexCycle and national project 6G-life, both focusing on next-generation robotic systems and human-machine collaboration. He previously held a postdoctoral position at TUM and the German Aerospace Center (DLR) and conducted extended doctoral research at the PRISMA Lab, University of Naples Federico II, Italy.



Moein Forouhar received the M.Sc. degree in Mechanical Engineering from Sharif University of Technology, Tehran, Iran, in 2016. He is currently a Ph.D. candidate at the Technical University of Munich (TUM) and a Research Associate at the Geriatrics Research Center in Garmisch-Partenkirchen, affiliated with the Munich Institute of Robotics and Machine Intelligence (MIRMI). His research focuses on tactile and cable-driven exoskeletons, teleoperation, and whole-body control of service robots for caregiving applications.



Abdeldjalil Naciri received the Ph.D. degree in Robotics from the University of Genoa, Italy, in 2011, in collaboration with the Italian Institute of Technology. He is currently a Senior Scientist and Team Lead at the Munich Institute of Robotics and Machine Intelligence (MIRMI), Technical University of Munich. His research interests include human-robot interaction, robotic manipulation, teleoperation, and safety-driven digital twins, with a focus on healthcare and service robotics applications.



Sami Haddadin received the Ph.D. degree in Electrical Engineering from RWTH Aachen University, Germany, in 2011. He is currently the Vice President of Research at Mohamed Bin Zayed University of Artificial Intelligence, Abu Dhabi, UAE. He was previously a Full Professor at the Technical University of Munich and the Founding Director of the Munich Institute of Robotics and Machine Intelligence (MIRMI). His research focuses on robotics, physical human-robot interaction, and AI-driven systems. He is the founder of Franka Emika and a recipient of multiple international research awards.